Photon-Assisted Tunneling in Carbon Nanotube Optical Rectennas: Characterization and Modeling

Erik C. Anderson[1*] and Baratunde A. Cola[1,2]

[1]*George W. Woodruff School of Mechanical Engineering, Georgia Institute of Technology, Atlanta, GA 30313, USA.*
[2]*School of Materials Science and Engineering, Georgia Institute of Technology, Atlanta, GA 30313, USA.*

Keywords: Metal–insulator–metal diodes, multiwall carbon nanotubes, optical rectenna, vertical CNT arrays

ABSTRACT

This paper presents optical characterization and modeling of carbon nanotube (CNT) rectennas featuring multi-insulator metal-insulator-metal tunneling diodes. The diodes use four layers of Al_2O_3 and ZrO_2 dielectric to obtain strong nonlinearity and highly asymmetric current density at low turn-on voltage. The CNT rectenna devices show energy conversion in the full optical spectrum (404 – 980 nm). We introduce the theory of photon-assisted tunneling (PAT) to model the optical behavior based off the unilluminated diode characteristics. Our model shows agreement between PAT and our experimental results, and fitting suggests a wavelength-dependent optical voltage. We discuss the impact of rectenna parameters and elucidate performance limits to our CNT rectenna device.

1. INTRODUCTION

Optical rectennas have been garnering attention with promises of enhanced efficiency in visible and infrared energy conversion[1–6], photodetection[7,8], heat transfer and low utility waste heat harvesting[4,9,10], and wireless power transmission[1,11]. Carbon-based nanomaterials are particularly interesting for high frequency rectennas owing to their low cost, high mobility, and optical properties[3,12–14]. For use in optical rectennas, graphene is an ideal material for geometric diodes and bowtie antennas[12,15,16]. The transparency and exceptional conductivity also makes graphene an attractive electrode material[14,17,18].

Multiwalled carbon nanotubes (CNTs) make exemplary dipole antenna elements, motivated by the extraordinary facility of CNTs to absorb electromagnetic energy in a broad spectrum[19–22]

* eanderson@gatech.edu

and ability to be easily fabricated in vertically aligned arrays[23,24]. As the CNT nanoantennas operate at infrared and visible frequencies, light-matter interaction governs the conversion of optical waves into a localized electrical field through each antenna[19,25]. Our current understanding of the CNT antennas is based on radio frequency (RF) dipole antenna theory, which may have limitations when operating near the CNT plasmon frequency[11,25].

Optical rectification mandates a high-speed diode capable of converting the oscillating electric field in the antenna into d.c. photocurrent. The metal-insulator-metal (MIM) tunneling diode satisfies the ultra-fast (femtosecond) switching time required for Terahertz rectification[26,27]. A MIM diode is a thin film technology composed of two electrodes separated by an insulator to create a potential energy barrier. Electron conduction is governed by nonlinear quantum tunneling through the barrier. Dissimilar electrodes form a gradient in the potential barrier that produces asymmetric *I–V* response[28].

The operating regime of a rectenna is established by the cutoff frequency of the diode: $f_c = \frac{1}{2\pi R_A C_D}$, given in terms of antenna resistance R_A and diode capacitance C_D. Ultra-small capacitance poses a problem for most rectenna devices[29]. We fabricate the diode at the tip of our CNTs, where the CNT tip serves as both antenna and the lower metal junction. The CNT-Insulator-Metal (CIM) diode concept mitigates antenna-to-diode ohmic loss, and more importantly, the ultra-small tip area ensures attofarad capacitance[3].

Since the work function difference between CNT and air-stable metals (here we use Al) is too low to generate enough asymmetry for optical rectification, manipulating the tunneling barrier via the insulator is needed. Tunneling diodes that combine multiple dielectrics have shown favorable performance over single-insulator diodes through more control of electron tunneling[30–32].

This works expands on our prior study of CIM diodes that investigated multilayers of Al_2O_3 and ZrO_2 to enhance diode properties[33]. We recently showed that more insulating layers generally enhanced the rectification ratio (i.e. asymmetry, $A = \left|\frac{I(+V)}{I(-V)}\right|$) without significantly affecting zero-bias resistance relative to a single-insulator device of comparable thickness. The disparity between electron affinities ($\chi(Al_2O_3)$~1.7 eV, $\chi(ZrO_2)$~2.7 eV)[34–36] facilitates resonant or step tunneling mechanisms that alter electron conduction[31,32,37]. Improving step tunneling produces a greater forward current at lower bias while suppressing reverse bias current.

In this study we use our best diode structure, a quad-insulator (CI^{4}M) diode with insulator stack composed of $Al_2O_3/ZrO_2/Al_2O_3/ZrO_2$, to demonstrate optical rectification over the full visible spectrum. The theory of photon-assisted tunneling (PAT) is applied to our measurements to model the CNT rectenna behavior and better understand the rectification mechanism and its ramifications.

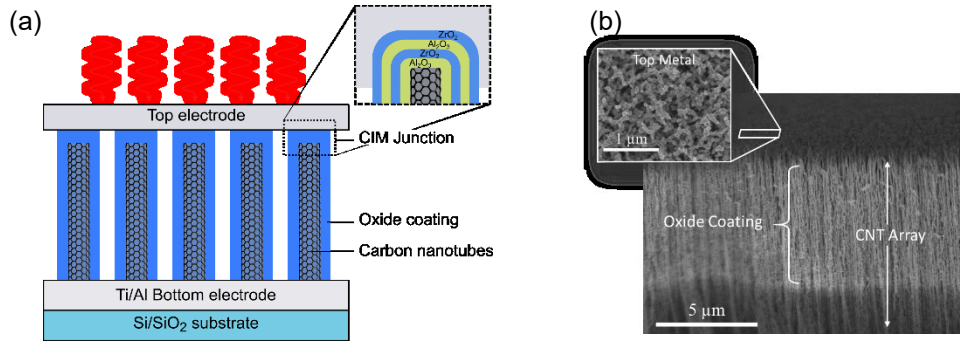

Figure 1. (a) A schematic of the carbon nanotube rectenna device. (Inset) The tips of the CNTs are coated in a quad-insulator laminate of dielectric and capped with Al top metal electrode to form a CNT/quad-Insulator/Metal (CI^{4}M) tunneling diode. (b) SEM sideview of the CNT array coated with oxide and top metal. The oxide penetrates several microns into the array while conformally coating the CNTs. (Inset) The top metal coating the array is not planar, but rather forms an interdigitated network of metal-coated CNTs with gaps between.

2. THEORY

We use the Tien-Gordon approach of photon-assisted tunneling to elucidate the effect of illumination in our rectenna devices[38]. The derivation of PAT for rectification has been rigorously covered in several other recent publications[39,40]. Here an overview of PAT is provided with more detail included in Supporting Information.

Upon illumination, the a.c. signal produced in the antenna causes a modulation in the Fermi level of the diode tunneling barrier. The overall voltage across the diode under high frequency monochromatic light is $\tilde{V}_{diode} = V + V_\omega \cos(\omega t)$. V is the d.c. (i.e. dark) bias applied to the diode and V_ω is the a.c. voltage modulation induced by the light. Under PAT, we consider the quantization of the light, wherein an electron absorbs or emits a discrete number of photons, n, each with energy $\hbar\omega$. This is reflected as a shift in the d.c. current-voltage response, $I_D(V)$, by a multiple of the photon voltage, $V_{ph} = \hbar\omega/e$. The photon-assisted (i.e. light) current, $I_L(V)$ is then the sum of all contributions of photon-assisted electron states, weighed by the nth order Bessel function $J_n(\alpha)$:

$$I_L(V) = \sum_{n=-\infty}^{\infty} J_n^2(\alpha)\, I_D\left(V + nV_{ph}\right). \quad (1)$$

The argument $\alpha = \frac{eV_\omega}{\hbar\omega} = \frac{V_\omega}{V_{ph}}$ is a measure of the a.c. field strength. For quantum operation, where $V_\omega < V_{ph}$ (i.e. $\alpha < 1$), only the n = 0, ±1 Bessel terms are significant. For a diode with sufficient asymmetry and low turn-on voltage, the summation of the modulated *I–V* curves allows positive current to flow under zero bias and provides power generation in the second quadrant. In practice, the illuminated *I–V* would vary from the prediction of PAT. Due to the frequency dependent optical properties of the diode materials, significant deviation in the shape and magnitude of the illuminated curves could be expected. PAT theory predicts rectification in

terms of the d.c. *I–V* behavior of the diode, although high frequency *I–V* characteristics are more appropriate, where it not for measurement impracticality.

The rectification process can be simplified to an equivalent electronic circuit by considering the antenna as an a.c. source in parallel with the diode[7,40]. The antenna source voltage, i.e. the optical voltage V_{opt}, depends on the input power to the antenna, P_{in}, and antenna radiation resistance R_A as

$$V_{opt} = \sqrt{8P_{in}R_A} \tag{2}$$

The a.c. voltage across the diode dependents on this source voltage and the bias dependent diode resistance. Therefore, in the case of constant input power, V_ω will vary as a function of applied bias. For an ideal linear diode, V_ω ranges from $V_{opt}/2$ to V_{opt}[39,41]. Under quantum operation this gives a convex hump in the second quadrant of the illuminated *I–V* that leads to more efficient energy conversion.

3. EXPERIMENTAL METHODS

3.1.Device Fabrication:

Carbon nanotube rectenna devices were fabricated using similar methods to previous reports[3,33,42] (Figure 1(a)). Multiwall carbon nanotubes were grown on high resistance Si coated with SiO_2 for electrical isolation. Ti/Al/Fe (100/10/3 nm) was deposited as the bottom electrode with Fe acting as the CNT catalyst. The vertical array of CNTs was then grown using low-pressure chemical vapor deposition with C_2H_2 carbon source gas (Aixtron Black Magic). Growth time around 180 s produces an array with heights around 10–30 μm, 8 nm diameter, and ~6 walls (Figure 1(b)). To expose the inner multiwalls, the CNT tips were etched away with 30 s of O_2 plasma at 80 W. The etched CNT array was conformally coated in multiple oxide layers by atomic layer deposition at 250 ºC. Layers were formed by cycling precursors of trimethylaluminum (for Al_2O_3) or tetrakis(dimethylamide) zirconium (for ZrO_2) along with H_2O vapors. Extended purge times were used so precursors could infiltrate the CNT array, giving an average coating of 4 nm per 40 cycles. The top electrode metal was 50 nm planar equivalent of Al deposited using thermal evaporation to minimize penetration through the oxide. 7 mm^2 device area was patterned with a shadow mask.

3.2.Characterization:

Electrical characterization was performed using a Keithley 2450 source monitor connected to a d.c. electrical 4-probe station. Optical characterization was performed using monochromatic laser diodes connected to a thermoelectrically cooled mount (Thorlabs TCLDM9). Wavelengths from 404 nm (742 THz) to 980 nm (306 THz) were passed through a diffuser to produce uniform illumination over the device and minimize potential thermoelectric effects. All electrical and optical measurements were performed in air at room temperature.

4. Results and Discussion

4.1.Dark Measurements

For this work, we use CI^{4}M rectenna devices composed of 16 nm total insulator thickness of $Al_2O_3/ZrO_2/Al_2O_3/ZrO_2$ quad-insulator laminate. We discussed previously that the CIM electrical behavior can be manipulated by altering the geometry of the tunneling barrier[33]. A thinner barrier exponentially lowers resistance, though at the expense of reduced nonlinearity and asymmetry, as well as fabrication limitations[42,43]. However, we simultaneously achieve high asymmetry and low resistance in our CI^{4}M diodes.

In Figure 2 we show the diode electrical response, i.e. the dark *I–V* rectenna characteristics. Step tunneling enhances forward bias current while suppressing reverse bias current to produce excellent diode properties suitable for optical rectification: asymmetry surpassing 300 and high nonlinearity beginning at a low turn-on voltage below 0.3 V (Figure S1). Peak responsivity is 6 A/W. Despite the overall low conductivity, a consequence of the high thickness of insulation used, this structure gives superior device stability and favorable rectification parameters.

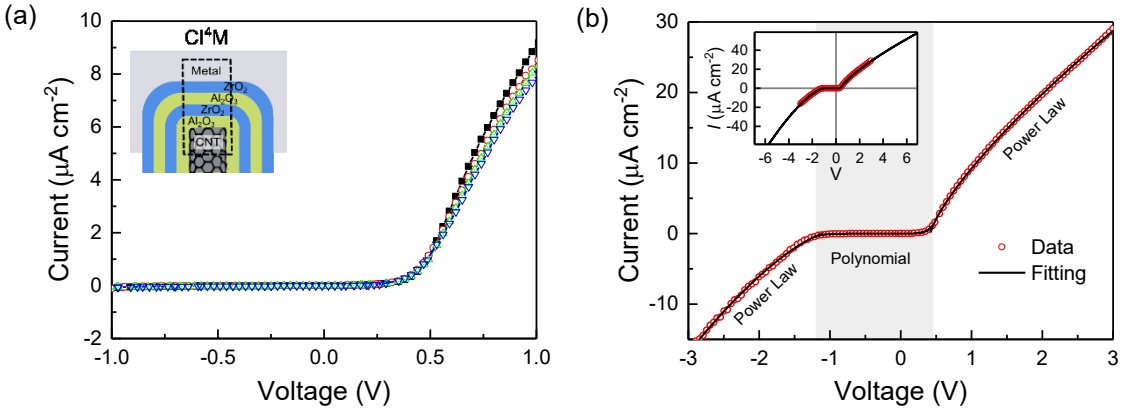

Figure 2. Dark *I–V* characteristics of CI^{4}M device with 16 nm $Al_2O_3/ZrO_2/Al_2O_3/ZrO_2$ insulator. Multiple repeat scans are shown to demonstrate scan consistency and stability over several days. Devices were very stable when scanning from ±1 V. (b) Fitting and extrapolation of dark *I–V* scans. Scanning from ±3 V shows a negative bias turn-on at –1 V, though higher bias caused more scan instability and likelihood of device failure. (Inset) Extrapolation past ±6 V was done by fitting a power law to each of the turned-on positive and negative bias regimes.

4.2.Optical Measurements

Here we present optical measurements of our CI^{4}M rectenna devices across the visible spectrum. Devices are illuminated with 5 mW/cm^2 incident power over a wavelength range of 404 – 980 nm (Figure 3(a-b)). *I–V* characteristics show a large increase in the forward bias current under illumination and a shift into the second quadrant, both indicators of the

rectification mechanism. The rectified photocurrent is proportional to the second derivative of current over ±0.5 V, providing additional evidence of rectification (Figure S2).

The optical response exhibits wavelength dependence, though the trend is not monotonic with photon energy. The effect of wavelength will be explored in depth in the next section. For the wavelengths tested, we see the maximum performance occurring at 638 nm: open-circuit voltage is V_{oc} = -95 mV short-circuit current is I_{sc} = 7.5 nA/cm^2; in terms of incident intensity total conversion efficiency is equal to $\eta = 3.6\times10^{-6}$ %. Due to unknown power losses, such as transmission through the top electrode, conversion efficiency will be left in terms of measured incident input power. Still, efficiency is low primarily from large resistance associated with the 16 nm thick insulator that was chosen to maximize asymmetry, device stability, and breakdown voltage. On the other hand, open-circuit voltage response is 250 V/W, 30 times larger than the double-insulator CI^{2}M rectenna reported previously[42]. These devices are thus great potential candidates for photodetection despite the low current.

Figure 3(c-d) shows a rise in current that scales with illumination intensity. Light-matter interactions in the CNT antenna cause a dependency of optical source voltage on incident power, which ultimately affects the optical response through V_ω[29]. The measured response is very stable with time (Figure 3(d)) with instantaneous on/off switching.

There is widespread concern that temperature gradients could induce thermal voltages that may be misconstrued for rectification[44,45]. In the Supporting Information (Figure S3) we provide evidence to rule out thermal behavior using an IR camera to measure surface temperature across an illuminated device. We did not observe a significant temperature gradient that would lead us to expect thermal effects.

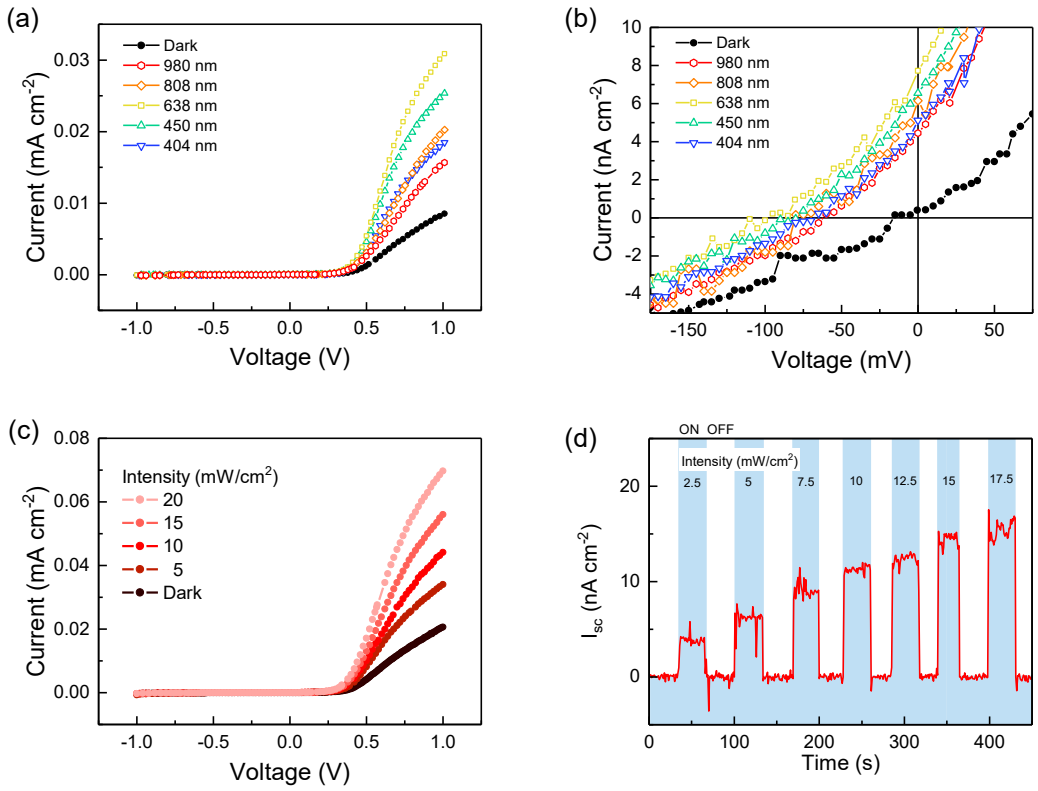

Figure 3. (a) Rectenna *I–V* characteristics under illumination with a wavelength range of 404 – 980 nm. Incident power is fixed at 5 mW/cm^2 with a diffuser used to illuminate uniformly over the device area. (b) High-resolution *I–V* scans near zero bias. The increase in forward bias current and second quadrant power generation are evidence of optical rectification. (c-d) *I–V* curves and short-circuit current, I_{sc}, with varying input power (λ = 638 nm). (d) Shows the measurement stability over time and is well above the noise threshold.

4.3.Photon-Assisted Tunneling Characterization

In this section we use PAT theory to model the illuminated *I–V* rectenna based off our diode's dark *I–V* behavior according to equation (1). Modeling the light characteristics with high photon energy (E_{ph}~3 eV at λ = 404 nm) requires diode *I–V* scanned over a correspondingly large bias. We managed to scan ±3 V before reaching device breakdown. A sufficient *I–V* window for PAT convergence calls for extrapolation. Power Law fitting was implemented to separately fit the high-bias positive and negative *I–V* regimes and extrapolate the dark current past ±7 V (Figure 2). This can accommodate Bessel terms at least to order 2.

Unlike the photon voltage which we readily control, V_{opt} and V_{ω} are difficult to estimate in our PAT prediction because of uncertainty with input parameters. There are several questionable assumptions associated with the optical voltage, namely, the actual power that is absorbed by the CNTs as well as likelihood for wavelength-dependent radiation resistance. More importantly, devices are practically expected to operate under constant input power mode, which leads to

bias-dependent V_ω[41]. We use our model to fit the PAT equation for V_ω and compare expected values in order to elucidate loss mechanisms and gain a better understanding of our CNT rectenna behavior. Initially, we assume constant V_ω that is not bias dependent. However, we realize the devices should practically operate under constant power instead of constant a.c. voltage. Indeed, a better fit to illuminated *I–V* data is achieved by introducing a mild, linear bias dependency in V_ω. The rationale of this trend will be made clear later by estimating V_ω from the semiclassical a.c. diode resistance.

A comparison of the rectification response for experimental data versus the PAT prediction is shown in Figure 4 for 638 nm light. The fixed a.c. diode voltage of $V_\omega = 68$ mV is found from fitting (Figure 4(a)). Photon energy of 1.94 eV gives quantum operation ($\alpha = 0.035$) and Bessel terms up to fourth order were used, keeping error from truncating higher order terms below 1 %. The model demonstrates reduction in zero-bias resistance and lowering of responsivity that is expected[3]. Still, the model underestimates the current, e.g. the secant resistance $R_{sec} = \frac{V_{oc}}{I_{sc}}$ predicted by PAT is distinctly higher than our experimental data.

By fitting $V_\omega(V)$, we achieve excellent agreement between illuminated *I–V* scans and the PAT prediction (Figure 4(b)). In the case of $\lambda = 638$ nm, V_ω varies from 58 mV at V_{oc} = -95 mV to 81 mV at zero bias. This supports the idea that these devices operate under a constant input power condition rather than constant a.c. voltage condition.

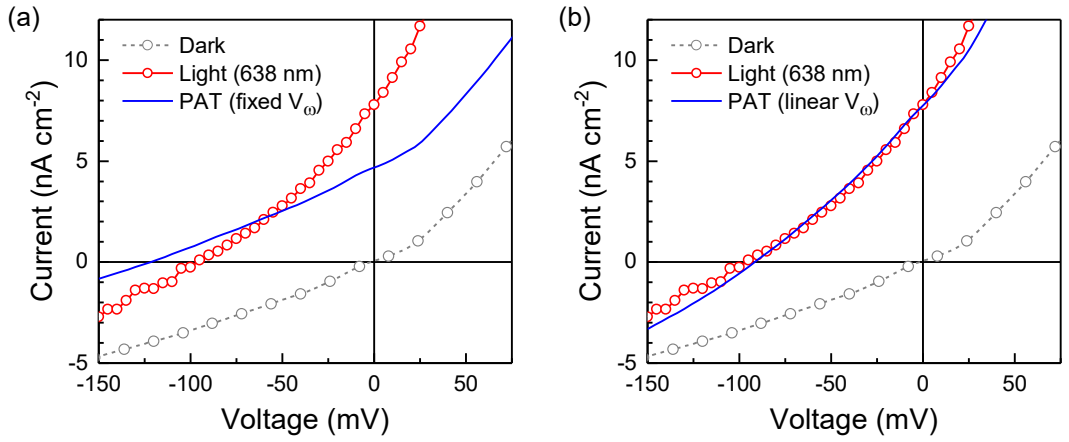

Figure 4. High-resolution *I–V* behavior of the rectification response at λ = 638 nm and 5 mW/cm^2 intensity. Markers represent dark (black) and light (red) scan data. (a) The predicted optical response (blue line) based on the theory of photon-assisted tunneling was determined by treating the diode voltage, V_ω, as a constant parameter and fitting to the light scan data. In the case of 638 nm, the PAT model yielded $V_\omega = 68$ mV. (b) A better prediction of the optical response was achieved by assuming bias-dependent V_ω (i.e. constant power operation). Fitting for $V_\omega(V)$ gives a mildly linearly trend from 58 mV at V_{oc} to 81 mV at zero bias.

Under constant power mode, the diode voltage varies with applied bias according to the a.c. resistance of the diode, $R_\omega(V)$ as[41]

$$V_\omega(V) = \sqrt{2P_{in}R_\omega(V)}.$$

For quantum operation ($\alpha \ll 1$), considering only first order Bessel terms gives an approximation for the a.c. diode resistance[41]:

$$R_\omega(V) = \frac{2V_{ph}}{I_D(V + V_{ph}) - I_D(V - V_{ph})}.$$

We show an exemplary calculation of $R_\omega(V)$ and corresponding estimation of $V_\omega(V)$ for 404 nm (3.07 eV) light in Supporting Information (Figure S5), which operates in the quantum regime. Qualitatively, there is a linear variation in V_ω with bias, which is an artifact of our dark *I–V* behavior. However, we do not know the actual input power nor any potential wavelength dependent losses. Also, at lower photon energy the legitimacy of using first order approximation for R_ω is questionable. Therefore, in fitting PAT theory to our results we preserve V_ω as an unknown parameter while assuming linearity. This is reasonable when trying to fit for the small bias window between V_{oc} and I_{sc}.

There is still discrepancy with the fitting model over larger scan range (e.g. 1 V), though the ability of the PAT to predict current at such bias is unreliable since it is primarily relies on extrapolated dark *I–V*. Aside from uncertainty from extrapolation, deviation in the model may be due to a variation in the optical and electrical material properties of the diode at terahertz frequencies. The fundamental tunneling characteristics of the diode would be different at high frequency, especially for multi-insulator structures. One would need to know the high frequency *I–V* of the isolated diode in place of the d.c. *I–V*, though this is impractical.

We next apply the PAT model to illustrate how both photon energy and input power affect the optical response. For wavelength-dependent optical excitation, the diode voltage is estimated by assuming bias dependence and individually fitting the PAT model to the *I–V* of each wavelength that was tested (Figure 5). We find less significant bias variation as the photon energy is lowered. This is expected as the system transitions into more classical behavior.

We use a simple spline to interpolate wavelength-dependent V_ω through photon energy up to 3.5 eV. From Figure 5, a linear trend of $V_\omega(V_{ph})$ is observed. The likely explanation is that the CNTs act as dipole antennas. Prior to this study, we assumed our antenna resistance was around 100 Ω, consistent with the literature.[3,7,25,46,47] Unlike bowtie antennas,[12,15,48,49] our CNTs likely act as dipole nanoantennas such that R_A will change with frequency. Classically, the resistance of a dipole is proportional to the frequency squared, i.e. $R_A \propto V_{ph}^2$.[50] Our definition of V_{opt} in equation (2) therein suggests that the antenna voltage increases linearly with photon energy for a dipole antenna, which would proportionately affect V_ω in the diode. However, there is limited understanding in how our CNT antenna array functions. For instance, at optical frequencies the plasmonic properties become important. The fact that the CNT array is not uniform lends further difficulty to estimating R_A; the array is a tangle of CNTs that are neither perfectly vertically aligned nor of equal length over large areas. Also, because the array is closely packed we expect strong diffusive scattering from nearby antenna interactions[51] that may screen the CNTs and

reduce field enhancement ordinarily seen in high aspect ratio CNTs[52]. Thus, a full understanding of the CNT antenna behavior at optical frequencies is necessary to gain a complete picture of the rectification mechanism.

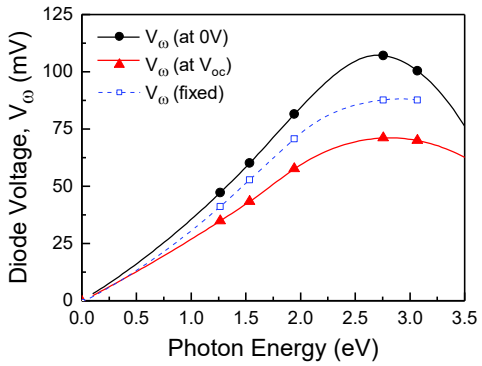

Figure 5. Diode voltage, V_ω, is determined by fitting the PAT model to illumination I(V) data for constant power operation (solid lines). The figure shows how the diode voltage varies with bias by depicting $V_\omega(V)$ at V_{oc} and I_{sc}. Cubic splines (solid lines) are used to interpolate V_ω across the wavelength range for use in the PAT model. V_ω under constant voltage operation is shown (open squares) for reference.

From our estimated $V_\omega(V_{ph})$, PAT theory generates peaks in V_{oc} and I_{sc} around 2.2 eV, expectedly corresponding to our measurements (Figure 6). For comparison, considering wavelength independent V_ω produces a maximum V_{oc} and I_{sc} are in the infrared, around 0.8 eV (1550 nm). The latter result is attributed to the reverse bias turn-on voltage of the diode suppressing rectification asymmetry. When photon energy exceeds this reverse bias turn-on there is no longer asymmetric tunneling of photon-assisted electrons, and hence the a.c. current passing through the diode is no longer rectified. In the case of fixed V_ω, rectenna performance could be enhanced by manipulating the diode *I–V* to suppress reverse bias turn-on.

On the other hand, introducing wavelength dependence into V_ω shifts the overall performance to higher photon energy in the visible regime. Rather than acting as an artifact of the diode *I–V*, we suspect the peak occurring at 2.2 eV arises after surpassing the diode's cutoff frequency: when the frequency of illumination exceeds f_c the diminishing antenna-diode coupling efficiency leads the drop off in performance. If this is the case, then one solution to improve the operating regime is by lowering capacitance to increase f_c.

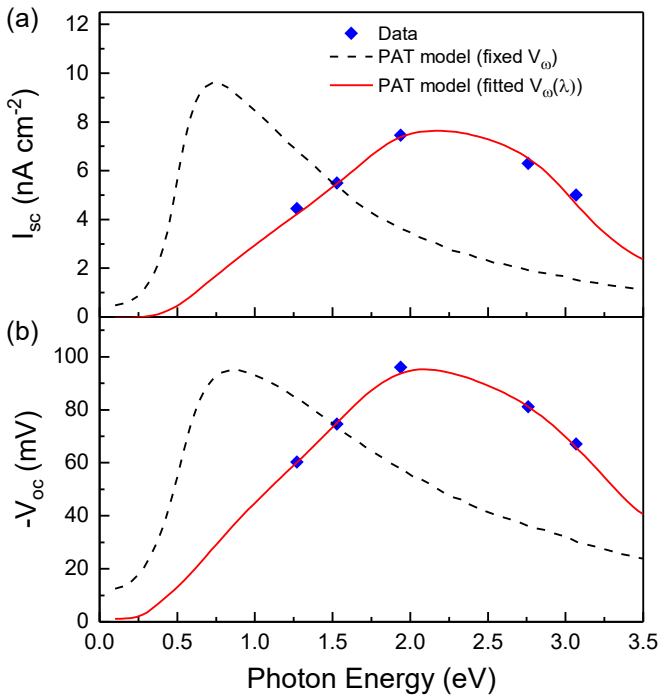

Figure 6. Comparison of PAT theory and measured (a) short-circuit current, I_{sc}, and (b) open-circuit voltage, V_{oc}. Blue diamonds show experimental data points; the dashed line shows the simulated PAT model with wavelength-independent diode voltage, using 808 nm as the reference wavelength from Figure 5 ($V_\omega = 60$ mV at 0 V bias); the solid line shows the PAT model with $V_\omega(\lambda)$ fitted at each wavelength.

The peak predicted optical conversion efficiency of 3.6×10^{-6} % is comparable to our prior reports[3,42] (see Table S1). We suspect that the actual input power absorbed by the CNTs is much less than the power we measure as incident upon the device surface. Even though rectenna conversion efficiency is still low, V_{oc} is large enough to give these CNT devices potential use as photodetectors. The V_{oc} here is several orders of magnitude higher than the first CNT rectenna reported by Sharma, *et al.*, which used a single insulator capped with Ca to produce low work function asymmetry[3]. Further, the open-circuit voltage response observed here is 30 times higher than the most recent report using a double-insulator diode structure[42], accredited to the improvement with the quad-insulator device structure[33]. However, low current remains a hindrance to overall efficiency. I_{sc} is lower than prior reports due to the high diode resistance associated with 16 nm thick insulation. Since this report is focused on understanding how our rectenna devices operate in light of photon-assisted tunneling, the choice of a thick insulator is subsequently based on the excellent diode stability and broad scanning bias range.

Next, we determine the effect of light intensity on illumination response by applying PAT theory through a range of incident laser powers according to equation (2). Figure 7 shows I_{sc} and V_{oc} at the representative wavelength of 638 nm (1.94 eV). There is excellent agreement between measurements and theory. Since the input power drives the optical voltage, greater laser intensity increases the rectified power generated in the second quadrant. The linear dependence between

I_{sc} and incident power shown in Figure 7(a) further supports optical rectification, owing to the fact that rectified current should be proportional to power delivered to the diode[7]. This is also consistent with the enhanced photocurrent we observed in Figure 3(c)[45]. The short-circuit current response is 1.5 μA/W. In contrast, V_{oc} approximately depends upon the square root of incident power. The open-circuit voltage response is 250 V/W at 5 mW/cm^2. This V_{oc} relationship heuristically follows the power dependent optical voltage that drives photon-assisted tunneling.

We point out that the input power of the PAT prediction displayed in Figure 7 was scaled to coincide with the experimental data. If antenna resistance around 100 Ω is assumed, then equation (2) predicts laser power several orders of magnitude lower than our measured incident power to fit PAT to the data. There is inevitable power loss associated with transmission of the incident radiation into the array and absorption by the CNT antennas. We estimate transmissivity of the Al electrode is below 6 % and with a mild wavelength dependence (Figure S6). Accounting for transmission would be misleading since there are complications such as the light transmitting through gaps in the top metal coating (see inset of Figure 1(b)). Other power loss mechanisms, for instance the antenna efficiency, can only be speculated but likely have significantly adverse effects on our present device performance.

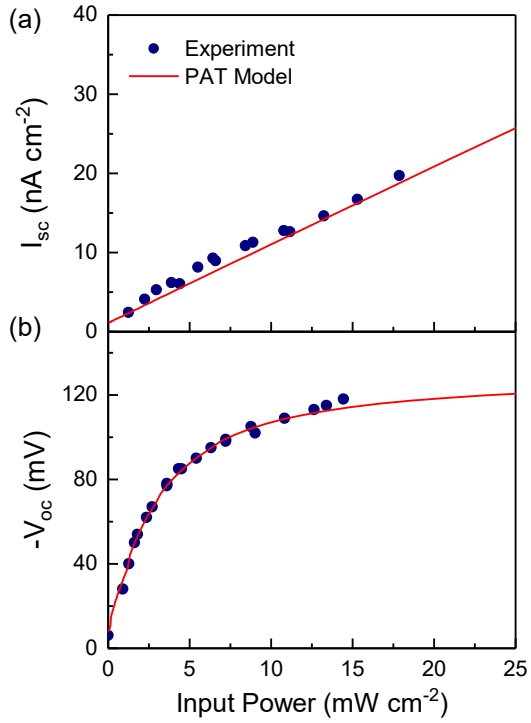

Figure 7. Power dependence on (a) Short-circuit current (I_{sc}) and (b) open-circuit voltage (V_{oc}) at a wavelength of 404 nm. Comparison of experimental data versus the PAT model is shown with the input power for the PAT model scaled to fit the experimental data.

Based on PAT, efficiency can be improved by optimizing the diode voltage under constant a.c. power. This requires tuning the dark *I–V* to affect the semiclassical resistance. Engineering

the diode *I–V* is perhaps the most direct route to better rectenna efficiency. Low turn-on voltage enables efficient operation at lower photon energy, whereas suppressing the reverse bias current will minimize loss at high photon energy. Maximizing the diode conductivity generally leads to better response across the board. Though a thinner tunneling barrier will significantly reduce the diode resistance, the effect on capacitance and therefore the cutoff frequency cannot be neglected. Making the electrodes more transparent yet conductive is still essential to mitigate optical and ohmic power losses. Lastly, better understanding of the CNT array as antenna elements is needed to optimize the optical voltage through antenna efficiency and radiation resistance.

5. CONCLUSIONS

We have provided evidence for rectification in the full range of optical frequencies using a carbon nanotube rectenna array. A quad-insulator tunneling diode is used to generate excellent diode asymmetry with a low turn-on suitable for rectification.

Photon-assisted tunneling theory is used to model the illuminated behavior of light based on the dark *I–V* measurements. We used the model to match predictions to experimental measurements of illuminated behavior across the optical spectrum. Our predictions provide further evidence of the rectification method in our CNT rectenna devices. By fitting the model to experiment we estimate the diode voltage and gain insight into several rectenna parameters of interest. The PAT prediction better matches experimental measurements when we assume bias-variable a.c. diode voltage under fixed input power operation. We also see a deviation with wavelength that can be accounted for through a combination of frequency-dependent optical voltage, antenna-diode coupling efficiency loss near cutoff frequency, and frequency dependent dielectric properties. We use this model to assess performance limits and determine areas of improvement for future generations of devices. The current structure has a peak performance around 638 nm with V_{oc} exceeding -95 mV and $\eta \sim 3.6\times10^{-6}$ %. Our model suggest that this could be improved by engineering the diode with lower resistance and capacitance, suppressing the reverse-bias current, and using top electrode materials that maximize light collection into the CNT array. Further refinement of the rectenna model is needed to understand and accurately depict operation of the CNT antenna at optical frequencies and any frequency dependence therein.

Author Information

Corresponding Author:
Email: eanderson@gatech.edu
Note:

Georgia Tech has applied for a patent, application no. PCT/US2013/065918, related to the design methods and materials produced in this work.

Acknowledgement

This work was supported by the National Science Foundation Graduate Research Fellowship Program (no. DGE-1650044) and the Alan T. Waterman Award (no. 1748413). The authors thank the staff of the Institute for Electronics and nanotechnology at Georgia Institute of Technology for providing training on and assistance with equipment. E.C.A. particularly thanks Dr. Thomas L. Bougher for assistance with the photon-assisted tunneling code and for many useful discussions.

REFERENCES

(1) Donchev, E.; Pang, J. S.; Gammon, P. M.; Centeno, A.; Xie, F.; Petrov, P. K.; Breeze, J. D.; Ryan, M. P.; Riley, D. J.; Alford, N. M. The Rectenna Device: From Theory to Practice (a Review). *MRS Energy Sustain.* **2014**, *1*, E1. https://doi.org/10.1557/mre.2014.6.

(2) Joshi, S.; Moddel, G. Simple Figure of Merit for Diodes in Optical Rectennas. *IEEE J. Photovoltaics* **2016**, *6* (3), 668–672. https://doi.org/10.1109/JPHOTOV.2016.2541460.

(3) Sharma, A.; Singh, V.; Bougher, T. L.; Cola, B. A. A Carbon Nanotube Optical Rectenna. *Nat. Nanotechnol.* **2015**, *10* (12), 1027–1032. https://doi.org/10.1038/nnano.2015.220.

(4) Jayaswal, G.; Belkadi, A.; Meredov, A.; Pelz, B.; Moddel, G.; Shamim, A. A Zero-Bias, Completely Passive 28 THz Rectenna for Energy Harvesting from Infrared (Waste Heat). In *IEEE MTT-S International Microwave Symposium Digest*; IEEE, 2018; pp 355–358. https://doi.org/10.1109/MWSYM.2018.8439447.

(5) Sabaawi, A. M. A.; Tsimenidis, C. C.; Sharif, B. S. Analysis and Modeling of Infrared Solar Rectennas. *IEEE J. Sel. Top. Quantum Electron.* **2013**, *19* (3), 9000208–9000208. https://doi.org/10.1109/JSTQE.2012.2227686.

(6) Sayed, I. E. H. Infrared Solar Energy Harvesting Using Nano-Rectennas. **2015**, No. September.

(7) Sanchez, A.; Davis, C. F.; Liu, K. C.; Javan, A. The MOM Tunneling Diode: Theoretical Estimate of Its Performance at Microwave and Infrared Frequencies. *J. Appl. Phys.* **1978**, *49* (10), 5270–5277. https://doi.org/10.1063/1.324426.

(8) Hobbs, P. C. D.; Laibowitz, R. B.; Libsch, F. R.; LaBianca, N. C.; Chiniwalla, P. P. Efficient Waveguide-Integrated Tunnel Junction Detectors at 1.6 Mm. *Opt. Express* **2007**, *15* (25), 16376. https://doi.org/10.1364/OE.15.016376.

(9) Shank, J.; Kadlec, E. A.; Jarecki, R. L.; Starbuck, A.; Howell, S.; Peters, D. W.; Davids, P. S. Power Generation from a Radiative Thermal Source Using a Large-Area Infrared Rectenna. *Phys. Rev. Appl.* **2018**, *9* (5), 54040. https://doi.org/10.1103/PhysRevApplied.9.054040.

(10) Strandberg, R. Theoretical Efficiency Limits for Thermoradiative Energy Conversion. *J. Appl. Phys.* **2015**, *117* (5). https://doi.org/10.1063/1.4907392.

(11) Novotny, L.; Van Hulst, N. Antennas for Light. *Nat. Photonics* **2011**, *5* (2), 83–90. https://doi.org/10.1038/nphoton.2010.237.

(12) Zhu, Z.; Joshi, S.; Grover, S.; Moddel, G. Graphene Geometric Diodes for Terahertz Rectennas. *J. Phys. D. Appl. Phys.* **2013**, *46* (18). https://doi.org/10.1088/0022-3727/46/18/185101.

(13) Matsumoto, K. *Frontiers of Graphene and Carbon Nanotubes*; 2015. https://doi.org/10.1007/978-4-431-55372-4.

(14) Ellmer, K. Past Achievements and Future Challenges in the Development of Optically Transparent Electrodes. *Nat. Photonics* **2012**, *6* (12), 809–817. https://doi.org/10.1038/nphoton.2012.282.

(15) Joshi, S.; Zhu, Z.; Grover, S.; Moddel, G. Infrared Optical Response of Geometric Diode Rectenna Solar Cells. In *Conference Record of the IEEE Photovoltaic Specialists Conference*; 2012; pp 2976–2978.

https://doi.org/10.1109/PVSC.2012.6318209.
(16) Yao, Y.; Kats, M. A.; Genevet, P.; Yu, N.; Song, Y.; Kong, J.; Capasso, F. Broad Electrical Tuning of Graphene-Loaded Plasmonic Antennas. *Nano Lett.* **2013**, *13* (3), 1257–1264. https://doi.org/10.1021/nl3047943.
(17) Zhou, Y.; Fuentes-Hernandez, C.; Shim, J.; Meyer, J.; Giordano, A. J.; Li, H.; Winget, P.; Papadopoulos, T.; Cheun, H.; Kim, J.; et al. A Universal Method to Produce Low-Work Function Electrodes for Organic Electronics. *Science (80-.).* **2012**, *336* (6079), 327–332. https://doi.org/10.1126/science.1218829.
(18) Wang, X.; Zhi, L.; Müllen, K. Transparent, Conductive Graphene Electrodes for Dye-Sensitized Solar Cells. *Nano Lett.* **2008**, *8* (1), 323–327. https://doi.org/10.1021/nl072838r.
(19) He, X.; Fujimura, N.; Lloyd, J. M.; Erickson, K. J.; Talin, A. A.; Zhang, Q.; Gao, W.; Jiang, Q.; Kawano, Y.; Hauge, R. H.; et al. Carbon Nanotube Terahertz Detector. *Nano Lett.* **2014**, *14* (7), 3953–3958. https://doi.org/10.1021/nl5012678.
(20) Zhang, T. F.; Li, Z. P.; Wang, J. Z.; Kong, W. Y.; Wu, G. A.; Zheng, Y. Z.; Zhao, Y. W.; Yao, E. X.; Zhuang, N. X.; Luo, L. B. Broadband Photodetector Based on Carbon Nanotube Thin Film/Single Layer Graphene Schottky Junction. *Sci. Rep.* **2016**, *6* (1), 38569. https://doi.org/10.1038/srep38569.
(21) Kumar, S.; Nehra, M.; Kedia, D.; Dilbaghi, N.; Tankeshwar, K.; Kim, K. H. Carbon Nanotubes: A Potential Material for Energy Conversion and Storage. *Progress in Energy and Combustion Science*. Pergamon January 1, 2018, pp 219–253. https://doi.org/10.1016/j.pecs.2017.10.005.
(22) Ren, L.; Zhang, Q.; Pint, C. L.; Wójcik, A. K.; Bunney, M.; Arikawa, T.; Kawayama, I.; Tonouchi, M.; Hauge, R. H.; Belyanin, A. A.; et al. Collective Antenna Effects in the Terahertz and Infrared Response of Highly Aligned Carbon Nanotube Arrays. **2013**, *87* (16), 161401. https://doi.org/10.1103/PhysRevB.87.161401.
(23) Choi, W. B.; Bae, E.; Kang, D.; Chae, S.; Cheong, B.; Ko, J.; Lee, E.; Park, W. Aligned Carbon Nanotubes for Nanoelectronics. *Nanotechnology* **2004**, *15* (10), S512–S516. https://doi.org/10.1088/0957-4484/15/10/003.
(24) Jakubinek, M. B.; White, M. A.; Li, G.; Jayasinghe, C.; Cho, W.; Schulz, M. J.; Shanov, V. Thermal and Electrical Conductivity of Tall, Vertically Aligned Carbon Nanotube Arrays. *Carbon N. Y.* **2010**, *48* (13), 3947–3952. https://doi.org/10.1016/j.carbon.2010.06.063.
(25) Olmon, R. L.; Raschke, M. B. Antenna-Load Interactions at Optical Frequencies: Impedance Matching to Quantum Systems. *Nanotechnology*. IOP Publishing November 9, 2012, p 444001. https://doi.org/10.1088/0957-4484/23/44/444001.
(26) Shilpi; Bhatt, K.; Sandeep; Kumar, S.; Tripathi, C. C. Potential Challenges and Issues in Implementation of MIM Diodes for Rectenna Application. In *Proceedings of the International Conference on Inventive Communication and Computational Technologies, ICICCT 2017*; IEEE, 2017; pp 83–88. https://doi.org/10.1109/ICICCT.2017.7975164.
(27) Eliasson, B. Metal-Insulator-Metal Diodes For Solar Energy Conversion. *PhD Thesis, Univ. Color. Boulder* **2001**, 1–228.
(28) Simmons, J. G. Electric Tunnel Effect between Dissimilar Electrodes Separated by a Thin Insulating Film John. *J. Appl. Phys.* **1963**, *34* (6), 1793–1803. https://doi.org/10.1063/1.1702682.
(29) Moddel, G.; Grover, S. *Rectenna Solar Cells*; 2013; Vol. 9781461437. https://doi.org/10.1007/978-1-4614-3716-1.
(30) Grover, S.; Moddel, G. Engineering the Current-Voltage Characteristics of Metal-Insulator-Metal Diodes Using Double-Insulator Tunnel Barriers. *Solid. State. Electron.* **2012**, *67* (1), 94–99. https://doi.org/10.1016/j.sse.2011.09.004.
(31) Alimardani, N.; Conley, J. F. Step Tunneling Enhanced Asymmetry in Asymmetric Electrode Metal-Insulator-Insulator-Metal Tunnel Diodes. *Appl. Phys. Lett.* **2013**, *102* (14), 1–6. https://doi.org/10.1063/1.4799964.
(32) Singh, A.; Ratnadurai, R.; Kumar, R.; Krishnan, S.; Emirov, Y.; Bhansali, S. Fabrication and Current-Voltage Characteristics of NiOx/ZnO Based MIIM Tunnel Diode. *Appl. Surf. Sci.* **2015**, *334*, 197–204. https://doi.org/10.1016/j.apsusc.2014.09.160.
(33) Anderson, E. C.; Bougher, T. L.; Cola, B. A. High Performance Multi-Insulator Carbon Nanotube Tunnel Diode Arrays. In *Proceedings of the 16th International Heat Transfer Conference*; Beijing, China, 2018; pp 1–8. https://doi.org/10.1002/aelm.201700446.
(34) Alimardani, N.; Conley, J. F. Enhancing Metal-Insulator-Insulator-Metal Tunnel Diodes via Defect Enhanced Direct Tunneling. *Appl. Phys. Lett.* **2014**, *105* (8), 1–6. https://doi.org/10.1063/1.4893735.
(35) Alimardani, N.; King, S. W.; French, B. L.; Tan, C.; Lampert, B. P.; Conley, J. F. Investigation of the

Impact of Insulator Material on the Performance of Dissimilar Electrode Metal-Insulator-Metal Diodes. *J. Appl. Phys.* **2014**, *116* (2), 024508. https://doi.org/10.1063/1.4889798.
(36) Kukli, K.; Kemell, M.; Vehkamäki, M.; Heikkilä, M. J.; Mizohata, K.; Kalam, K.; Ritala, M.; Leskelä, M.; Kundrata, I.; Fröhlich, K. Atomic Layer Deposition and Properties of Mixed Ta 2 O 5 and ZrO 2 Films. *AIP Adv.* **2017**, *7* (2), 025001. https://doi.org/10.1063/1.4975928.
(37) Weerakkody, A. D.; Sedghi, N.; Mitrovic, I. Z.; Van Zalinge, H.; Nemr Noureddine, I.; Hall, S.; Wrench, J. S.; Chalker, P. R.; Phillips, L. J.; Treharne, R.; et al. Enhanced Low Voltage Nonlinearity in Resonant Tunneling Metal-Insulator-Insulator-Metal Nanostructures. *Microelectron. Eng.* **2015**, *147*, 298–301. https://doi.org/10.1016/j.mee.2015.04.110.
(38) Tien, P. K.; Gordon, J. P. Multiphoton Process Observed in the Interaction of Microwave Fields with the Tunneling between Superconductor Films. *Phys. Rev.* **1963**, *129* (2), 647–651. https://doi.org/10.1103/PhysRev.129.647.
(39) Joshi, S.; Moddel, G. Optical Rectenna Operation: Where Maxwell Meets Einstein. *J. Phys. D. Appl. Phys.* **2016**, *49* (26), 265602. https://doi.org/10.1088/0022-3727/49/26/265602.
(40) Joshi, S.; Moddel, G. Rectennas at Optical Frequencies: How to Analyze the Response. *J. Appl. Phys.* **2015**, *118* (8), 1–6. https://doi.org/10.1063/1.4929648.
(41) Grover, S.; Joshi, S.; Moddel, G. Quantum Theory of Operation for Rectenna Solar Cells. *J. Phys. D. Appl. Phys.* **2013**, *46* (13), 135106. https://doi.org/10.1088/0022-3727/46/13/135106.
(42) Anderson, E. C.; Bougher, T. L.; Cola, B. A. High Performance Multiwall Carbon Nanotube–Insulator–Metal Tunnel Diode Arrays for Optical Rectification. *Adv. Electron. Mater.* **2018**, *4* (3), 1700446. https://doi.org/10.1002/aelm.201700446.
(43) Shah, E. H.; Brown, B.; Cola, B. A. A Study of Electrical Resistance in Carbon Nanotube-Insulator-Metal Diode Arrays for Optical Rectenna. *IEEE Trans. Nanotechnol.* **2017**, *16* (2), 230–238. https://doi.org/10.1109/TNANO.2017.2656066.
(44) Tu, X. W.; Lee, J. H.; Ho, W. Atomic-Scale Rectification at Microwave Frequency. *J. Chem. Phys.* **2006**, *124* (2), 021105. https://doi.org/10.1063/1.2159491.
(45) Ward, D. R.; HÜser, F.; Pauly, F.; Cuevas, J. C.; Natelson, D. Optical Rectification and Field Enhancement in a Plasmonic Nanogap. *Nat. Nanotechnol.* **2010**, *5* (10), 732–736. https://doi.org/10.1038/nnano.2010.176.
(46) Zhu, Z.; Joshi, S.; Grover, S.; Moddel, G. Geometric Diodes for Optical Rectennas. In *Rectenna Solar Cells*; Springer New York: New York, NY, 2013; Vol. 9781461437, pp 209–227. https://doi.org/10.1007/978-1-4614-3716-1_10.
(47) Grover, S.; Dmitriyeva, O.; Estes, M. J.; Moddel, G. Traveling-Wave Metal/Insulator/Metal Diodes for Improved Infrared Bandwidth and Efficiency of Antenna-Coupled Rectifiers. *IEEE Trans. Nanotechnol.* **2010**, *9* (6), 716–722. https://doi.org/10.1109/TNANO.2010.2051334.
(48) Gadalla, M. N.; Abdel-Rahman, M.; Shamim, A. Design, Optimization and Fabrication of a 28.3â€...THz Nano-Rectenna for Infrared Detection and Rectification. *Sci. Rep.* **2014**, *4*, 4270. https://doi.org/10.1038/srep04270.
(49) Fischer, H.; Martin, O. J. F. Engineering the Optical Response of Plasmonic Nanoantennas. *Opt. Express* **2008**, *16* (12), 9144. https://doi.org/10.1364/OE.16.009144.
(50) Eggleston, M. S.; Messer, K.; Zhang, L.; Yablonovitch, E.; Wu, M. C. Optical Antenna Enhanced Spontaneous Emission. *Proc. Natl. Acad. Sci.* **2015**, *112* (6), 1704–1709. https://doi.org/10.1073/pnas.1423294112.
(51) Kempa, K.; Rybczynski, J.; Huang, Z.; Gregorczyk, K.; Vidan, A.; Kimball, B.; Carlson, J.; Benham, G.; Wang, Y.; Herczynski, A.; et al. Carbon Nanotubes as Optical Antennae. *Adv. Mater.* **2007**, *19* (3), 421–426. https://doi.org/10.1002/adma.200601187.
(52) Milne, W. I.; Teo, K. B. K.; Amaratunga, G. A. J.; Legagneux, P.; Gangloff, L.; Schnell, J.-P.; Semet, V.; Thien Binh, V.; Groening, O. Carbon Nanotubes as Field Emission Sources. *J. Mater. Chem.* **2004**, *14* (6), 933. https://doi.org/10.1039/b314155c.
(53) Briones, E.; Briones, J.; Martinez-Anton, J. C.; Cuadrado, A.; McMurtry, S.; Hehn, M.; Montaigne, F.; Alda, J.; González, J. Seebeck Nanoantennas for Infrared Detection and Energy Harvesting Applications. *9th Eur. Conf. Antennas Propag.* **2014**, *1* (June).
(54) Li, L. Study of Metal-Insulator-Metal Diodes for Photodetection, 2013.

Supporting Information

Photon-Assisted Tunneling in Carbon Nanotube Optical Rectennas: Characterization and Modeling

Erik C. Anderson[1*] and Baratunde A. Cola[1,2]

[1]George W. Woodruff School of Mechanical Engineering, Georgia Institute of Technology, Atlanta, GA 30313, USA.
[2]School of Materials Science and Engineering, Georgia Institute of Technology, Atlanta, GA 30313, USA.

[*] eanderson@gatech.edu

S.1. DARK *I–V* CURVES

Dark *I–V* characteristics of our CI[4]M diode are shown in Figure S1. The device features low turn-on voltage at 0.23 V with rectification asymmetry exceeding 200. Asymmetry ($A = \left|\frac{I(+V)}{I(-V)}\right|$) peaks to 245 at 0.8 V. Around -1 V there is another turn-on point which increases reverse-bias current causing a reduction in asymmetry. Responsivity, defined in terms of the first and second derivative of the current with respect to voltage ($S = \frac{1}{2}I''/I'$), is important in energy harvesting as the value describes the change in current per unit absorbed power. Here, responsivity peaks at 6.1 A/W with zero-bias responsivity of 4.3 A/W. The zero-bias resistance is 10^7 Ω·cm^2, which is much higher than the thinner insulator devices reported in[42] owing to the 16 nm total insulation and the Al top metal contact. Despite the resistance, this device was selected due it its high asymmetry, nonlinearity ($N = \frac{I'}{I/V}$), and low turn-on voltage, all of which contribute to excellent scan stability and rectification across the full optical spectrum.

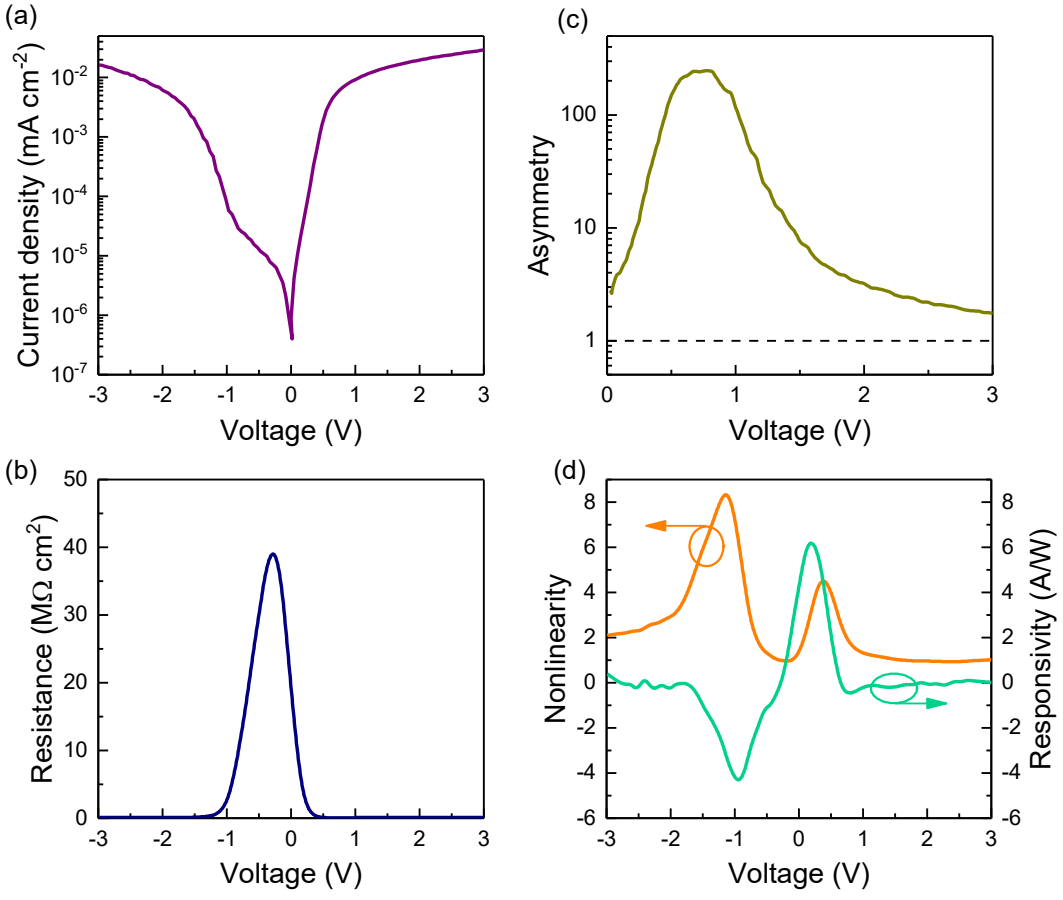

Figure S1. Electrical characterization of the CI[4]M diode. (a) current density, (b) resistance, (c) asymmetry, (d) nonlinearity and responsivity, all shown as a function of bias.

S.2. 2ND DERIVATIVE AS EVIDENCE FOR OPTICAL RECTIFICATION

In the presence of a radiation-induced a.c. voltage oscillation, $V_\omega \cos(\omega t)$, the total current through the tunneling diode can be approximated to the first order by[7,44]

$$I_L(V) \approx I_D(V) + \frac{1}{4} V_\omega^2 \left(\frac{d^2 I}{dV^2} \right). \quad \text{(S1)}$$

The overall measured current under illumination is comprised of the unilluminated d.c. current I_D and rectification photocurrent current, $I_R(V) = \frac{1}{4} V_\omega^2 \left(\frac{d^2 I}{dV^2} \right)$. The major assumption here is that the conduction mechanism is unaffected by the a.c. oscillation. The validity of this relation can be confirmed by comparing the rectified current to d^2I/dV^2; proportionality to the second derivative would then reveal the a.c. optical voltage. Figure S2 shows a comparison of the rectified current at $\lambda = 980$ nm compared to d^2I/dV^2. The second derivative shows good agreement with the illuminated *I–V*. We suppose that the deviation at higher bias can be due to the limits of the first order approximation of optical rectification.

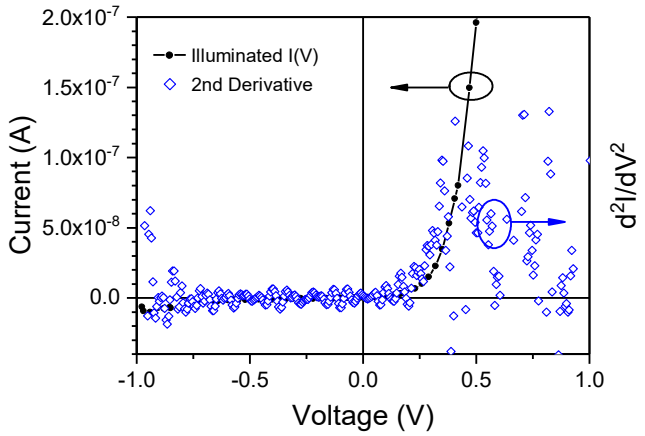

Figure S2. CNT rectenna device under 980 nm illumination. The 2nd derivative is computed from high-order numerical approximation of the illuminated I(V) scan. The 2nd derivative is scaled to overlay with the illuminated I(V) scan. The agreement between the I(V) and d^2I/dV^2 is additional evidence for optical rectification.

S.3. RULING OUT THERMOELECTRIC RESPONSE

We used an infrared camera to capture the temperature rise under 100 mW laser power (~5 mm^2 spot size). Undiffused laser power only caused 2 ºC temperature differential (Figure S3(a-c)) along the device, and there was barely any temperature rise when using the diffuser. In principle, metallic CNTs should have zero Seebeck coefficient[19]. Even if there was a thermoelectric effect between any of the metal layers or the substrate, the observed temperature

difference would result in a V_{oc} far smaller than our measured optical response[53]. Further, our use of a diffuser throughout *I–V* measurements would further mitigate any substantial temperature gradient that might cause thermoelectric effects. Devices were also heated with a heat gun (without illumination) to show that heating the sample does not produce a significant thermal voltage (Figure S3(c)). We thus rule out thermally-induced behavior in our observed response.

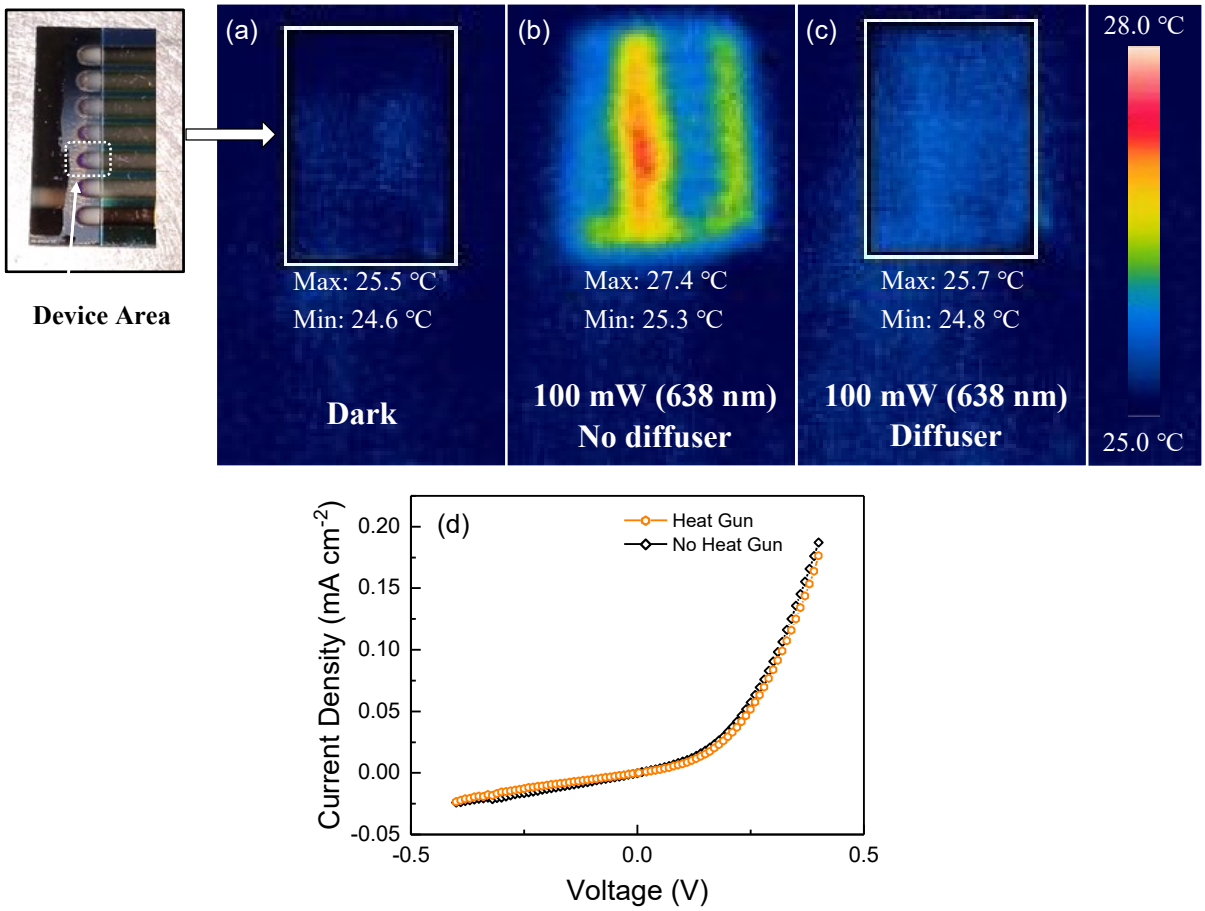

Figure S3. (a-c) Infrared images of the rectenna device under 100 mW illumination (λ = 638 nm) show only 2 °C temperature rise with direct laser beam and no significant temperature change under a diffuser. (d) *I–V* scan of the rectenna device when heated with a heat gun versus the unheated dark scan. There is no significant change from the heat gun, nor a shift into the second quadrant, providing further evidence that illumination testing shows rectification and not a thermoelectric response.

S.4. PHOTON-ASSISTED TUNNELING THEORY

Incident illumination captured by an adjacent antenna source creates an oscillating voltage in addition to the d.c. bias across a diode: $\tilde{V}_{diode} = V_{dc} + \tilde{V}(\omega)$. Treating the current in the diode as the quantum tunneling of individual electrons through a thin potential barrier, we consider the

oscillation, $\tilde{V}(\omega) = V_\omega \cos(\omega t)$, as a perturbation in the electron's original Hamiltonian, H_0. Based on the perturbed state, $H = H_0 + eV_\omega cos(\omega t)$, the new electronic wave function has the form

$$\psi(\vec{r}, t) = \psi(\vec{r}) e^{-\frac{iE_0 t}{\hbar}} \left(\sum B_n e^{-in\omega t} \right) \tag{S2}$$

which satisfies the Schrodinger Equation with the coefficients $B_n = J_n\left(\frac{eV_\omega}{\hbar\omega}\right)$, where J_n is the Bessel function of the first kind. The effect of illumination can be more clearly seen by combining the terms before the summation into the unperturbed state, $\psi_0(E_0)$, simplifying the wave function to

$$\psi(n, V_\omega) = \psi_0(E_0) \left(\sum_{n=-\infty}^{\infty} J_n\left(\frac{eV_\omega}{\hbar\omega}\right) e^{-\frac{i(n\hbar\omega)t}{\hbar}} \right). \tag{S3}$$

This suggests that a photon-assisted electron has a probability $J_n(eV_\omega/\hbar\omega)$ of possessing energy nħω above its unilluminated state. n signifies the number of photons absorbed or emitted by the electron in a multi-photon process[41]. The total wavefunction is the weighted sum of all possible states in n. The purpose of equation (S3) is mainly to elucidate the physical impact of the photon absorption relative to the original wavefunction. We can more easily arrive at an equation to describe the current in an illuminated device by distributing the unperturbed energy into the summation. Then the exponential terms may be absorbed into the argument of the original wavefunction:

$$\psi(n, V_\omega) = \sum_{n=-\infty}^{\infty} J_n(\alpha)\, \psi_0(E_0 + n\hbar\omega). \tag{S4}$$

Now it is clear that the photon-assisted electrons have shifted the original wavefunction to energy $E_0 + n\hbar\omega$. We use the substitution $\alpha = \frac{eV_\omega}{\hbar\omega}$ for the argument of the Bessel Function. The net electron current in a quantum system can be found from the wavefunctions through[54]

$$I = \frac{-e\hbar \mathrm{A}}{2m_e} [\psi^* \nabla\psi - \psi \nabla\psi^*]. \tag{S5}$$

A is the area, m_e is the electron effective mass, and ψ^* is the complex conjugate of the wavefunction. This relation must count all possible wavefunctions while weighing their respective probabilities, though this is already reflected in equation (S3) since we are indeed accounting for all electron states while the coefficients naturally satisfy normalization[38]. It should be clear that when using the wavefunction from equation (S4) that the illuminated tunneling current, I_L, will be found by shifting the dark current according to the newly prescribed electron energy and weighed by the square of the probability amplitude (i.e. $J_n^2(\alpha)$). We can express the unilluminated electron energy in terms of applied d.c. electrical potential, which we call V for consistency, and note that the photon energy is $V_{ph} = \hbar\omega/e$. Finally, the PAT theory gives illuminated current, I_L, in terms of the dark current, I_D, through

$$I_L(V) = \sum_{n=-\infty}^{\infty} J_n^2(\alpha)\, I_D\big(V + nV_{ph}\big). \tag{S6}$$

S.5. MODELING PHOTON-ASSISTED TUNNELING

We model the illuminated behavior of our rectenna device according to photon-assisted tunneling theory. To calculate the illuminated current from equation (S6), we use the dark *I–V* behavior of our diode from Figure 2 and Figure S1. We calculate $I_L(V)$ from equation (S6) using as many terms in the summation as the dark *I–V* scan window permits. Since our diode curves only go up to ±3 V, extrapolation is required in order to use PAT with high photon energy and higher order terms. As described in the main text, and shown in Figure 2, we extrapolate our diode *I–V* past ±7 V, enabling terms up to n = 2 at 3.5 eV photon energy. For low V_{ph} the results of PAT are independent of the extrapolation. Only for large photon energy ~2–3 eV does the extrapolation make a difference. However, since the behavior falls within the quantum regime at such photon energy ($\alpha \sim 0.03$), the first order Bessel terms dominate and error in the extrapolation is minor.

The PAT prediction also requires knowledge of V_ω. However, since we do not have a reliable estimate for the input power or the CNT antenna resistance we fit for V_ω based on our measured $I_L(V)$. We use the Levenberg-Marquardt algorithm for nonlinear least-squares fitting of the PAT equation to our measured light *I–V* response. This allows us to determine V_ω for each wavelength we tested.

S.6. VERIFICATION OF PHOTON-ASSISTED TUNNELING MODEL

We check the validity of our PAT model by following the results reported in references [40,41]. Consider the case of an ideal, piecewise linear diode with zero reverse-bias current and a linear forward-bias current having a resistance of 50 Ω. We assume antenna resistance is 100 Ω and diode voltage $V_\omega = V_{opt}/2$. With low photon energy of 4 meV and power of 200 μW we get classical operation ($V_{opt} \gg V_{ph}$). Our PAT model gives such classical behavior (**Figure S4**(a))that matches previous PAT reports.[40] Not only does the piecewise diode shift into the second quadrant, there is a distinct nonlinearity that is induced by the response of the low energy light.

…

…

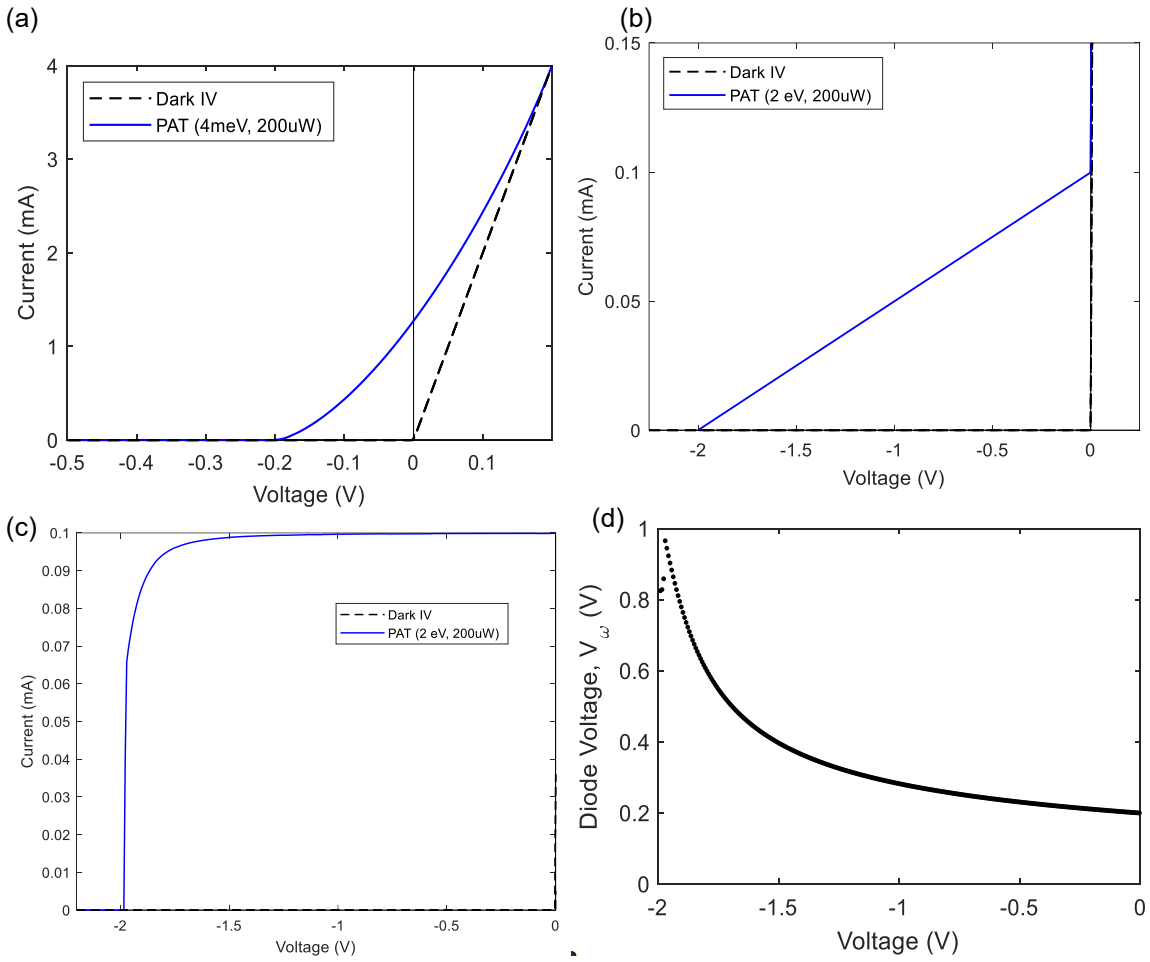

Figure S4. PAT Model verification using an ideal piecewise linear diode with 50 Ω forward resistance. (a) Classical operation at 4 meV and 200 μW ($\alpha = 50$). (b-d) Quantum operation at 2 eV and 200 μW ($\alpha = 0.1$). (b) Operation under fixed a.c. diode voltage $V_\omega = V_{opt}/2$ shows a linear region of second quadrant power generation. (c) Constant input power mode, wherein V_ω varies with bias. A convex hump in the second quadrant is formed due to the variable V_ω, which is depicted in (d) as a result of iteratively solving for the first harmonic of a.c. rectified current, I_ω. The diode voltage tends to $V_{opt}/2$ at zero bias.

S.7. DETERMINING V_ω FOR CONSTANT POWER OPERATION

We have so far assumed fixed V_ω. However, the devices should practically operate under constant power, which instead makes the diode voltage vary with applied bias according to the a.c. resistance of the diode, $R_\omega(V)$ as[41]

$$V_\omega(V) = \sqrt{2P_D R_\omega(V)}. \tag{S5}$$

P_D is the power coupled to the diode (i.e. the power delivered by the antenna to the diode)[7]. For quantum operation ($\alpha \ll 1$), considering only first order Bessel terms gives an approximation for the a.c. diode resistance[41]:

$$R_\omega(V) = \frac{2V_{ph}}{I_D(V + V_{ph}) - I_D(V - V_{ph})}. \quad \text{(S6)}$$

We show an exemplary calculation of $R_\omega(V)$ and corresponding estimation of $V_\omega(V)$ for 404 nm (3.07 eV) light (Figure S5), which operates semiclassically in the quantum regime. Qualitatively, there is a linear variation in V_ω with bias, which is an artifact of our dark *I–V*. However, we do not know the input power precisely nor potential wavelength-dependent absorption. Also, at lower photon energy the legitimacy of using the first order approximation for R_ω is questionable. Therefore, for fitting the PAT theory to our results we retain V_ω as an unknown parameter while still assuming linearity. We show in Figure S5 that this is reasonable when trying to fit for the behavior in the small bias window between V_{oc} and I_{sc}.

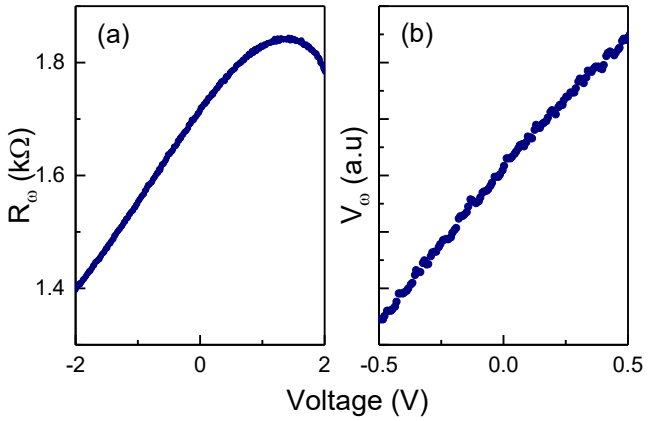

Figure S5. Estimation of the a.c. diode resistance, R_ω, using the semiclassical approximation at 404 nm (3.07 eV). The a.c. diode voltage, V_ω, varies linearly with bias and the numerical value depends on P_{in}.

S.8. TRANSPARENCY OF TOP METAL

The input power we use for efficiency calculations does not consider reflection and transmission through the top metal. In this section we attempt to account for transmission losses through the top metal to more accurately calculate our input power and hence, our conversion efficiency. We measured the transmission of 50 nm planar Al on glass in the range around 1-6 % (see Figure S6 for wavelength-dependent transmission).

We can adjust the conversion efficiency originally calculated by now accounting for power loss from wavelength-dependent transmission. This would boost our peak efficiency at 638 nm to 2.3×10^{-4} %. However, accounting for transmission did not fully make up the deviation between our measured input power and the PAT model. Additionally, there are other issues that make directly accounting for transmission problematic. First, the top metal coating on the CNT array is not planar (see SEM images from Figure 1(b)). Since some length of each CNT is coated

in metal, rather than just the very tip surface, the actual coating thickness could be less than 50 nm since it is distributed over a larger surface area.

Perhaps more important, we suspect that light may pass through gaps between the mesh of top metal-coated CNTs until finally being absorbed by uncoated segments of CNT deeper within the array. Then the actual input power to the CNT antennas may not be strictly related to the transparency of the top Al layer. To prevent erroneous calculations, we describe the input power using the laser intensity incident upon the surface; we do not adjust for reflection, transmission, absorption, etc., and instead note that all parameters and analyses related to device input power would have an additional efficiency associated with losses of the incoming electromagnetic waves.

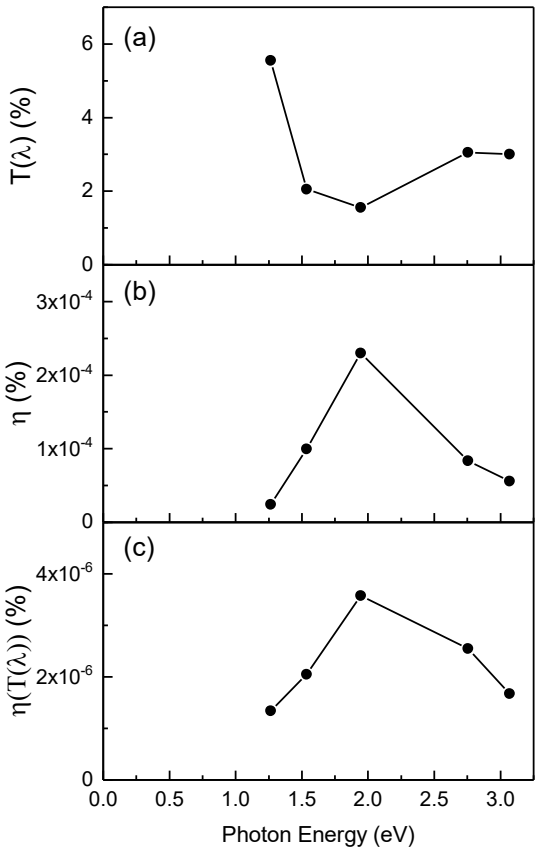

Figure S6. Impact of wavelength-dependent top metal transparency on efficiency calculations. (a) Plot of transmission as a function of photon energy for 50 nm Al deposited on a glass slide, used to estimate the actual input power to the rectenna device. Values were adjusted for the transmission losses due to the glass slide (~90%). Conversion efficiency measurements (b) without considering and (c) with considering wavelength-dependent top metal transparency.

S.9. DEPENDENCE OF α ON PHOTON ENERGY

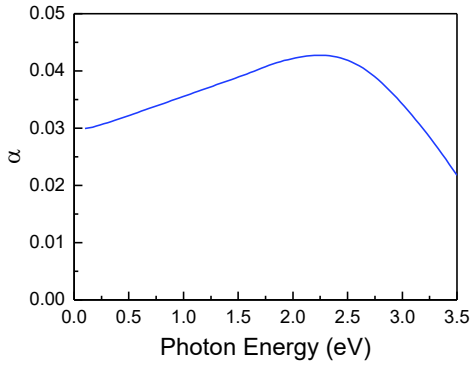

Figure S7. Illustration of the relationship between $\alpha = \frac{V_\omega}{V_{ph}}$ and the photon energy, V_{ph}. There is a peak occurring at 2.2 eV.

S.10. COMPARISON TO PRIOR CNT RECTENNA REPORTS

Table S1. Comparison of optical rectification performance for recent CNT optical rectenna publications. The device structure for each report are the following: (Sharma, *et al.*) CNT/Al_2O_3 (8 nm)/Ca; (Anderson, *et al.*) CNT/Al_2O_3-HfO_2 (4/4 nm)/Ag; and (This work) CNT/Al_2O_3-ZrO_2-Al_2O_3-ZrO_2 (4/4/4/4 nm)/Al.

Authors	Year	P_{in} (mW/cm^2)	λ (nm)	I_{sc} (nA/cm^2)	V_{oc} (mV)	η (%)	Current Response (A/W)	Voltage Response (V/W)
Sharma et al.	2015	26	532	1700	-0.16	$3\times10^{-7*}$	6.5×10^{-5}	4×10^{-3}
Anderson et al.	2018	20	638	500	-11	7×10^{-6}	2.5×10^{-5}	7.6
This work	2019	5	638	7.5	-95	3.6×10^{-6}	1.5×10^{-6}	250

*values not corrected for the 10% transmission estimation.

REFERENCES

(1) Donchev, E.; Pang, J. S.; Gammon, P. M.; Centeno, A.; Xie, F.; Petrov, P. K.; Breeze, J. D.; Ryan, M. P.; Riley, D. J.; Alford, N. M. The Rectenna Device: From Theory to Practice (a Review). *MRS Energy Sustain.* **2014**, *1*, E1. https://doi.org/10.1557/mre.2014.6.

(2) Joshi, S.; Moddel, G. Simple Figure of Merit for Diodes in Optical Rectennas. *IEEE J. Photovoltaics* **2016**, *6* (3), 668–672. https://doi.org/10.1109/JPHOTOV.2016.2541460.

(3) Sharma, A.; Singh, V.; Bougher, T. L.; Cola, B. A. A Carbon Nanotube Optical Rectenna. *Nat. Nanotechnol.* **2015**, *10* (12), 1027–1032. https://doi.org/10.1038/nnano.2015.220.

(4) Jayaswal, G.; Belkadi, A.; Meredov, A.; Pelz, B.; Moddel, G.; Shamim, A. A Zero-Bias, Completely Passive 28 THz Rectenna for Energy Harvesting from Infrared (Waste Heat). In *IEEE MTT-S International Microwave Symposium Digest*; IEEE, 2018; pp 355–358. https://doi.org/10.1109/MWSYM.2018.8439447.

(5) Sabaawi, A. M. A.; Tsimenidis, C. C.; Sharif, B. S. Analysis and Modeling of Infrared Solar Rectennas. *IEEE J. Sel. Top. Quantum Electron.* **2013**, *19* (3), 9000208–9000208.

https://doi.org/10.1109/JSTQE.2012.2227686.
(6) Sayed, I. E. H. Infrared Solar Energy Harvesting Using Nano-Rectennas. **2015**, No. September.
(7) Sanchez, A.; Davis, C. F.; Liu, K. C.; Javan, A. The MOM Tunneling Diode: Theoretical Estimate of Its Performance at Microwave and Infrared Frequencies. *J. Appl. Phys.* **1978**, *49* (10), 5270–5277. https://doi.org/10.1063/1.324426.
(8) Hobbs, P. C. D.; Laibowitz, R. B.; Libsch, F. R.; LaBianca, N. C.; Chiniwalla, P. P. Efficient Waveguide-Integrated Tunnel Junction Detectors at 1.6 Mm. *Opt. Express* **2007**, *15* (25), 16376. https://doi.org/10.1364/OE.15.016376.
(9) Shank, J.; Kadlec, E. A.; Jarecki, R. L.; Starbuck, A.; Howell, S.; Peters, D. W.; Davids, P. S. Power Generation from a Radiative Thermal Source Using a Large-Area Infrared Rectenna. *Phys. Rev. Appl.* **2018**, *9* (5), 54040. https://doi.org/10.1103/PhysRevApplied.9.054040.
(10) Strandberg, R. Theoretical Efficiency Limits for Thermoradiative Energy Conversion. *J. Appl. Phys.* **2015**, *117* (5). https://doi.org/10.1063/1.4907392.
(11) Novotny, L.; Van Hulst, N. Antennas for Light. *Nat. Photonics* **2011**, *5* (2), 83–90. https://doi.org/10.1038/nphoton.2010.237.
(12) Zhu, Z.; Joshi, S.; Grover, S.; Moddel, G. Graphene Geometric Diodes for Terahertz Rectennas. *J. Phys. D. Appl. Phys.* **2013**, *46* (18). https://doi.org/10.1088/0022-3727/46/18/185101.
(13) Matsumoto, K. *Frontiers of Graphene and Carbon Nanotubes*; 2015. https://doi.org/10.1007/978-4-431-55372-4.
(14) Ellmer, K. Past Achievements and Future Challenges in the Development of Optically Transparent Electrodes. *Nat. Photonics* **2012**, *6* (12), 809–817. https://doi.org/10.1038/nphoton.2012.282.
(15) Joshi, S.; Zhu, Z.; Grover, S.; Moddel, G. Infrared Optical Response of Geometric Diode Rectenna Solar Cells. In *Conference Record of the IEEE Photovoltaic Specialists Conference*; 2012; pp 2976–2978. https://doi.org/10.1109/PVSC.2012.6318209.
(16) Yao, Y.; Kats, M. A.; Genevet, P.; Yu, N.; Song, Y.; Kong, J.; Capasso, F. Broad Electrical Tuning of Graphene-Loaded Plasmonic Antennas. *Nano Lett.* **2013**, *13* (3), 1257–1264. https://doi.org/10.1021/nl3047943.
(17) Zhou, Y.; Fuentes-Hernandez, C.; Shim, J.; Meyer, J.; Giordano, A. J.; Li, H.; Winget, P.; Papadopoulos, T.; Cheun, H.; Kim, J.; et al. A Universal Method to Produce Low-Work Function Electrodes for Organic Electronics. *Science (80-.).* **2012**, *336* (6079), 327–332. https://doi.org/10.1126/science.1218829.
(18) Wang, X.; Zhi, L.; Müllen, K. Transparent, Conductive Graphene Electrodes for Dye-Sensitized Solar Cells. *Nano Lett.* **2008**, *8* (1), 323–327. https://doi.org/10.1021/nl072838r.
(19) He, X.; Fujimura, N.; Lloyd, J. M.; Erickson, K. J.; Talin, A. A.; Zhang, Q.; Gao, W.; Jiang, Q.; Kawano, Y.; Hauge, R. H.; et al. Carbon Nanotube Terahertz Detector. *Nano Lett.* **2014**, *14* (7), 3953–3958. https://doi.org/10.1021/nl5012678.
(20) Zhang, T. F.; Li, Z. P.; Wang, J. Z.; Kong, W. Y.; Wu, G. A.; Zheng, Y. Z.; Zhao, Y. W.; Yao, E. X.; Zhuang, N. X.; Luo, L. B. Broadband Photodetector Based on Carbon Nanotube Thin Film/Single Layer Graphene Schottky Junction. *Sci. Rep.* **2016**, *6* (1), 38569. https://doi.org/10.1038/srep38569.
(21) Kumar, S.; Nehra, M.; Kedia, D.; Dilbaghi, N.; Tankeshwar, K.; Kim, K. H. Carbon Nanotubes: A Potential Material for Energy Conversion and Storage. *Progress in Energy and Combustion Science*. Pergamon January 1, 2018, pp 219–253. https://doi.org/10.1016/j.pecs.2017.10.005.
(22) Ren, L.; Zhang, Q.; Pint, C. L.; Wójcik, A. K.; Bunney, M.; Arikawa, T.; Kawayama, I.; Tonouchi, M.; Hauge, R. H.; Belyanin, A. A.; et al. Collective Antenna Effects in the Terahertz and Infrared Response of Highly Aligned Carbon Nanotube Arrays. **2013**, *87* (16), 161401. https://doi.org/10.1103/PhysRevB.87.161401.
(23) Choi, W. B.; Bae, E.; Kang, D.; Chae, S.; Cheong, B.; Ko, J.; Lee, E.; Park, W. Aligned Carbon Nanotubes for Nanoelectronics. *Nanotechnology* **2004**, *15* (10), S512–S516. https://doi.org/10.1088/0957-4484/15/10/003.
(24) Jakubinek, M. B.; White, M. A.; Li, G.; Jayasinghe, C.; Cho, W.; Schulz, M. J.; Shanov, V. Thermal and Electrical Conductivity of Tall, Vertically Aligned Carbon Nanotube Arrays. *Carbon N. Y.* **2010**, *48* (13), 3947–3952. https://doi.org/10.1016/j.carbon.2010.06.063.
(25) Olmon, R. L.; Raschke, M. B. Antenna-Load Interactions at Optical Frequencies: Impedance Matching to Quantum Systems. *Nanotechnology*. IOP Publishing November 9, 2012, p 444001. https://doi.org/10.1088/0957-4484/23/44/444001.
(26) Shilpi; Bhatt, K.; Sandeep; Kumar, S.; Tripathi, C. C. Potential Challenges and Issues in Implementation of MIM Diodes for Rectenna Application. In *Proceedings of the International Conference on Inventive*

Communication and Computational Technologies, ICICCT 2017; IEEE, 2017; pp 83–88. https://doi.org/10.1109/ICICCT.2017.7975164.
(27) Eliasson, B. Metal-Insulator-Metal Diodes For Solar Energy Conversion. *PhD Thesis, Univ. Color. Boulder* **2001**, 1–228.
(28) Simmons, J. G. Electric Tunnel Effect between Dissimilar Electrodes Separated by a Thin Insulating Film John. *J. Appl. Phys.* **1963**, *34* (6), 1793–1803. https://doi.org/10.1063/1.1702682.
(29) Moddel, G.; Grover, S. *Rectenna Solar Cells*; 2013; Vol. 9781461437. https://doi.org/10.1007/978-1-4614-3716-1.
(30) Grover, S.; Moddel, G. Engineering the Current-Voltage Characteristics of Metal-Insulator-Metal Diodes Using Double-Insulator Tunnel Barriers. *Solid. State. Electron.* **2012**, *67* (1), 94–99. https://doi.org/10.1016/j.sse.2011.09.004.
(31) Alimardani, N.; Conley, J. F. Step Tunneling Enhanced Asymmetry in Asymmetric Electrode Metal-Insulator-Insulator-Metal Tunnel Diodes. *Appl. Phys. Lett.* **2013**, *102* (14), 1–6. https://doi.org/10.1063/1.4799964.
(32) Singh, A.; Ratnadurai, R.; Kumar, R.; Krishnan, S.; Emirov, Y.; Bhansali, S. Fabrication and Current-Voltage Characteristics of NiOx/ZnO Based MIIM Tunnel Diode. *Appl. Surf. Sci.* **2015**, *334*, 197–204. https://doi.org/10.1016/j.apsusc.2014.09.160.
(33) Anderson, E. C.; Bougher, T. L.; Cola, B. A. High Performance Multi-Insulator Carbon Nanotube Tunnel Diode Arrays. In *Proceedings of the 16th International Heat Transfer Conference*; Beijing, China, 2018; pp 1–8. https://doi.org/10.1002/aelm.201700446.
(34) Alimardani, N.; Conley, J. F. Enhancing Metal-Insulator-Insulator-Metal Tunnel Diodes via Defect Enhanced Direct Tunneling. *Appl. Phys. Lett.* **2014**, *105* (8), 1–6. https://doi.org/10.1063/1.4893735.
(35) Alimardani, N.; King, S. W.; French, B. L.; Tan, C.; Lampert, B. P.; Conley, J. F. Investigation of the Impact of Insulator Material on the Performance of Dissimilar Electrode Metal-Insulator-Metal Diodes. *J. Appl. Phys.* **2014**, *116* (2), 024508. https://doi.org/10.1063/1.4889798.
(36) Kukli, K.; Kemell, M.; Vehkamäki, M.; Heikkilä, M. J.; Mizohata, K.; Kalam, K.; Ritala, M.; Leskelä, M.; Kundrata, I.; Fröhlich, K. Atomic Layer Deposition and Properties of Mixed Ta 2 O 5 and ZrO 2 Films. *AIP Adv.* **2017**, *7* (2), 025001. https://doi.org/10.1063/1.4975928.
(37) Weerakkody, A. D.; Sedghi, N.; Mitrovic, I. Z.; Van Zalinge, H.; Nemr Noureddine, I.; Hall, S.; Wrench, J. S.; Chalker, P. R.; Phillips, L. J.; Treharne, R.; et al. Enhanced Low Voltage Nonlinearity in Resonant Tunneling Metal-Insulator-Insulator-Metal Nanostructures. *Microelectron. Eng.* **2015**, *147*, 298–301. https://doi.org/10.1016/j.mee.2015.04.110.
(38) Tien, P. K.; Gordon, J. P. Multiphoton Process Observed in the Interaction of Microwave Fields with the Tunneling between Superconductor Films. *Phys. Rev.* **1963**, *129* (2), 647–651. https://doi.org/10.1103/PhysRev.129.647.
(39) Joshi, S.; Moddel, G. Optical Rectenna Operation: Where Maxwell Meets Einstein. *J. Phys. D. Appl. Phys.* **2016**, *49* (26), 265602. https://doi.org/10.1088/0022-3727/49/26/265602.
(40) Joshi, S.; Moddel, G. Rectennas at Optical Frequencies: How to Analyze the Response. *J. Appl. Phys.* **2015**, *118* (8), 1–6. https://doi.org/10.1063/1.4929648.
(41) Grover, S.; Joshi, S.; Moddel, G. Quantum Theory of Operation for Rectenna Solar Cells. *J. Phys. D. Appl. Phys.* **2013**, *46* (13), 135106. https://doi.org/10.1088/0022-3727/46/13/135106.
(42) Anderson, E. C.; Bougher, T. L.; Cola, B. A. High Performance Multiwall Carbon Nanotube–Insulator–Metal Tunnel Diode Arrays for Optical Rectification. *Adv. Electron. Mater.* **2018**, *4* (3), 1700446. https://doi.org/10.1002/aelm.201700446.
(43) Shah, E. H.; Brown, B.; Cola, B. A. A Study of Electrical Resistance in Carbon Nanotube-Insulator-Metal Diode Arrays for Optical Rectenna. *IEEE Trans. Nanotechnol.* **2017**, *16* (2), 230–238. https://doi.org/10.1109/TNANO.2017.2656066.
(44) Tu, X. W.; Lee, J. H.; Ho, W. Atomic-Scale Rectification at Microwave Frequency. *J. Chem. Phys.* **2006**, *124* (2), 021105. https://doi.org/10.1063/1.2159491.
(45) Ward, D. R.; HÜser, F.; Pauly, F.; Cuevas, J. C.; Natelson, D. Optical Rectification and Field Enhancement in a Plasmonic Nanogap. *Nat. Nanotechnol.* **2010**, *5* (10), 732–736. https://doi.org/10.1038/nnano.2010.176.
(46) Zhu, Z.; Joshi, S.; Grover, S.; Moddel, G. Geometric Diodes for Optical Rectennas. In *Rectenna Solar Cells*; Springer New York: New York, NY, 2013; Vol. 9781461437, pp 209–227. https://doi.org/10.1007/978-1-4614-3716-1_10.
(47) Grover, S.; Dmitriyeva, O.; Estes, M. J.; Moddel, G. Traveling-Wave Metal/Insulator/Metal Diodes for Improved Infrared Bandwidth and Efficiency of Antenna-Coupled Rectifiers. *IEEE Trans. Nanotechnol.*

2010, *9* (6), 716–722. https://doi.org/10.1109/TNANO.2010.2051334.
(48) Gadalla, M. N.; Abdel-Rahman, M.; Shamim, A. Design, Optimization and Fabrication of a 28.3â€...THz Nano-Rectenna for Infrared Detection and Rectification. *Sci. Rep.* **2014**, *4*, 4270. https://doi.org/10.1038/srep04270.
(49) Fischer, H.; Martin, O. J. F. Engineering the Optical Response of Plasmonic Nanoantennas. *Opt. Express* **2008**, *16* (12), 9144. https://doi.org/10.1364/OE.16.009144.
(50) Eggleston, M. S.; Messer, K.; Zhang, L.; Yablonovitch, E.; Wu, M. C. Optical Antenna Enhanced Spontaneous Emission. *Proc. Natl. Acad. Sci.* **2015**, *112* (6), 1704–1709. https://doi.org/10.1073/pnas.1423294112.
(51) Kempa, K.; Rybczynski, J.; Huang, Z.; Gregorczyk, K.; Vidan, A.; Kimball, B.; Carlson, J.; Benham, G.; Wang, Y.; Herczynski, A.; et al. Carbon Nanotubes as Optical Antennae. *Adv. Mater.* **2007**, *19* (3), 421–426. https://doi.org/10.1002/adma.200601187.
(52) Milne, W. I.; Teo, K. B. K.; Amaratunga, G. A. J.; Legagneux, P.; Gangloff, L.; Schnell, J.-P.; Semet, V.; Thien Binh, V.; Groening, O. Carbon Nanotubes as Field Emission Sources. *J. Mater. Chem.* **2004**, *14* (6), 933. https://doi.org/10.1039/b314155c.
(53) Briones, E.; Briones, J.; Martinez-Anton, J. C.; Cuadrado, A.; McMurtry, S.; Hehn, M.; Montaigne, F.; Alda, J.; González, J. Seebeck Nanoantennas for Infrared Detection and Energy Harvesting Applications. *9th Eur. Conf. Antennas Propag.* **2014**, *1* (June).
(54) Li, L. Study of Metal-Insulator-Metal Diodes for Photodetection, 2013.